Progress in Propulsion Physics **4** (2013) 205-226
DOI: 10.1051/eucass/201304205
© Owned by the authors, published by EDP Sciences, 2013

SIMULATION OF SUPERCRITICAL FLOWS IN ROCKET-MOTOR ENGINES: APPLICATION TO COOLING CHANNEL AND INJECTION SYSTEM

G. Ribert, D. Taieb, X. Petit, G. Lartigue, and P. Domingo

CNRS — UMR 6614 — CORIA and INSA de Rouen
Campus du Madrillet, St-Etienne-du-Rouvray 76801, France

To address physical modeling of supercritical multicomponent fluid flows, ideal-gas law must be changed to real-gas equation of state (EoS), thermodynamic and transport properties have to incorporate dense fluid corrections, and turbulence modeling has to be reconsidered compared to classical approaches. Real-gas thermodynamic is presently investigated with validation by NIST (National Institute of Standards and Technology) data. Two major issues of Liquid Rocket Engines (LRE) are also presented. The first one is the supercritical fluid flow inside small cooling channels. In a context of LRE, a strong heat flux coming from the combustion chamber (locally $\phi \approx 80$ MW/m^2) may lead to very steep density gradients close to the wall. These gradients have to be thermodynamically and numerically captured to properly reproduce in the simulation the mechanism of heat transfer from the wall to the fluid. This is done with a shock-capturing weighted essentially nonoscillatory (WENO) numerical discretization scheme. The second issue is a supercritical fluid injection following experimental conditions [1] in which a trans- or supercritical nitrogen is injected into warm nitrogen. The two-dimensional results show vortex structures with high fluid density detaching from the main jet and persisting in the low-speed region with low fluid density.

1 INTRODUCTION

The suggestion to use supercritical fluids (SFs) for technical applications is a century old, but the main progress in investigating and utilizing SFs has occurred mainly in the past 20 years. They have been used (or proposed for use)

This is an Open Access article distributed under the terms of the Creative Commons Attribution License 2.0, which permits unrestricted use, distribution, and reproduction in any medium, provided the original work is properly cited.

Article available at http://www.eucass-proceedings.eu or http://dx.doi.org/10.1051/eucass/201304205

as solvents, reaction media, processing media, etc. In the present study, SFs are considered as propellants. Indeed, many fluid mechanical devices involve thermodynamic phase transition from a subcritical to a supercritical state. For example, the high-pressure combustion chambers of LRE operate at pressures and temperatures well above the critical points of the injected propellants, which consequently are in a supercritical state. Such engines operate at pressure, typically of the order of 10.0 MPa whereas the critical pressure of hydrogen and oxygen is, respectively, 1.3 and 5.0 MPa. Another example are jet engines of aircraft. In order to increase the efficiency and thus reduce the CO_2 emissions, a general trend to increased pressures in the combustion chamber can be observed as well as the development of special designs of combustion chambers (LPP: Lean-Premix-Prevaporize or RQL: Rich-Quench-Lean) to limit NOx production. As a consequence, the liquid fuel may be injected at supercritical conditions. Generally, the chamber pressure is above the critical pressure of the fuel ($p > p_c$) while the injection temperature is subcritical ($T < T_c$). For example, the critical properties of decane which is commonly used to simulate kerosene, are $p_c = 2.1$ MPa and $T_c = 617.7$ K. Such a state is called *compressed fluids* (or *transcritical* state [2]). After injection, the fuel heats up and its temperature exceeds its critical value ($T > T_c$). In both regimes, the fluid is neither a liquid nor a gas, but has liquid-like density along with gas-like properties; beyond the critical point (p_c, T_c), there is no distinction between gaseous and liquid phases. These points are summarized in Fig. 1. Most of the current understanding of turbulence and mixing is the result of atmospheric-pressure studies and numerous numerical and experimental databases are available. A similar work has to be undertaken for sub-, trans-, and supercritical flows.

A unified treatment of general fluid thermodynamic, valid for all these fluid states, is required [3, 4] to perform numerical simulation of such flows. The theoretical model for thermodynamics is based on the observation of Van der Waals that, for any pure species, the reduced pressure, $p_r = p/p_c$, is a universal

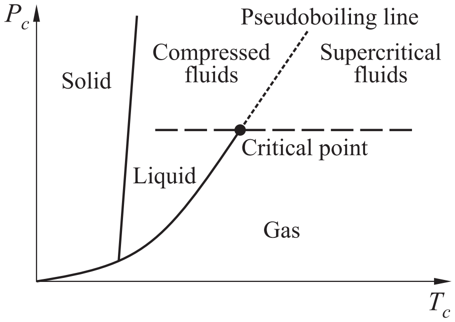

Figure 1 Pressure–temperature diagram with phase change curves

Table 1 Compressibility and acentric factors from [5, 6]

Substance	p_c, MPa	T_c, K	Z_c	ω
CO_2	7.38	304.1	0.274	0.239
H_2O	22.1	647.3	0.235	0.344
Ethane	4.88	305.4	0.285	0.099
Ethene	5.04	282.4	0.280	0.089
Propane	4.25	369.8	0.281	0.153
Xenon	5.84	289.7	0.287	0.008
O_2	5.04	154.6	0.288	0.025
H_2	1.3	33.2	0.303	−0.216
N_2	3.4	126.3	0.29	0.039

function of the reduced temperature, $T_r = T/T_c$, and molar volume, $v_r = v/v_c$. The law of corresponding states expresses that all pure gases have the same compressibility factor, Z, i. e., a variable measuring the deviation from ideal behavior, at the same values of reduced pressure and reduced temperature [5]. At the critical point, this value is $Z(p_c, T_c) = Z_c = 0.29$. The law of corresponding states may be also applied to any thermodynamic property. The experimental results match very well for species with symmetrical molecules (Xenon, for example) but requires another parameter, the acentric factor, ω, for nonsymmetric one (Table 1). The geometric description of molecules as well as their thermodynamic state are then crucial elements for LRE design and it will be studied in section 2. Transport equations will be described in section 3 and two examples of simulations of LRE issues (heat transfer and injection) are given in section 4.

2 THERMODYNAMIC

Fluid flow simulation requires the numerical resolution of the Navier–Stokes equations. For fluid flow with heat transfer, transport equations for mass, momentum and energy have to be considered leading to six unknown variables: density, ρ, the three components of velocity, u_i, total energy, for instance, e_t, and pressure, p. Thermodynamic variables p–ρ–T, T being the temperature, are linked together through the EoS which complete the system of equations.

2.1 Equation of State

It is well-known from experimental observations that the ideal-gas (PG) EoS is not valid for high-pressure, especially, near the critical point:

$$p = \rho r T \quad \text{with} \quad r = \frac{\mathcal{R}}{W} .$$

Table 2 Cubic EoS coefficients [5]

Equation	u	w	b	a	$\alpha(T,\omega)$
VDW	0	0	$\dfrac{\mathcal{R}T_c}{8P_c}$	$\dfrac{27}{64}\dfrac{\mathcal{R}^2T_c^2}{P_c}$	1
RK	1	0	$\dfrac{0.08664\mathcal{R}T_c}{P_c}$	$\dfrac{0.42748\mathcal{R}^2T_c^{2.5}}{P_c}$	$\dfrac{1}{T^{0.5}}$
SRK	1	0	$\dfrac{0.08664\mathcal{R}T_c}{P_c}$	$\dfrac{0.42748\mathcal{R}^2T_c^2}{P_c}$	$[1+f_{1\omega}(1-\sqrt{T_r})]^2\,;$ $f_{1\omega}=0.48+1.574\omega-0.176\omega^2$
PR	2	-1	$\dfrac{0.07780\mathcal{R}T_c}{P_c}$	$\dfrac{0.42748\mathcal{R}^2T_c^2}{P_c}$	$[1+f_{2\omega}(1-\sqrt{T_r})]^2\,;$ $f_{2\omega}=0.37464+1.54226\omega-0.26992\omega^2$

where $\mathcal{R}$ is the ideal gas constant and W is the mean molar mass of the mixture. Indeed, for ideal gases, short distance intermolecular force are negligible. However, increasing pressure, short-distance forces become important and in the supercritical state, short-distance interactions between molecules and the proper volume of molecules have to be taken into account to properly model the fluid behavior by an EoS. For flows in LREs, widely used equations are *cubic* EoS because they are a compromise between accuracy and time of calculation. These three-parameter equations include attractive forces among particles, a, covolume of particles, b, and acentric factor, ω, which quantifies the deviation from spherical symmetry in a molecule:

$$p=\frac{\mathcal{R}T}{v-b}-\frac{a\alpha(T,\omega)}{v^2+ubv+wb^2} \tag{1}$$

where v ($=W/\rho$) is the molar volume and α is the function depending on T and ω (Table 2) according to the chosen EoS. Introducing the compressibility factor, $Z=(pv)/(\mathcal{R}T)$, in the above equations leads to a cubic equation:

$$Z^3-(1+B-uB)Z^2+(A+wB^2-uB-uB^2)Z-AB-wB^2-wB^3=0 \tag{2}$$

where $A=(a\alpha p)/(\mathcal{R}^2T^2)$ and $B=(bp)/(\mathcal{R}T)$. In Eq. (2), Z quantifies the deviation from the ideal gas assumption; $Z=1$ for ideal gases. In Eq. (1), u and w depend on the model of EoS retained: VDW for Van der Waals, RK for Redlich–Kwong, SRK for Soave–Redlich–Kwong, and PR for Peng–Robinson. The VDW EoS is a two-parameter EoS as the acentric factor is taken equal to 1, thus limiting the range of application. Compared to experimental data of oxygen, Yang [7] shows an error of 13% and 17% for SRK and PR, respectively. Oefelein [8] recommends to use the PR EoS for simulations with strong heat release, but SRK EoS is much more precise for low temperature.

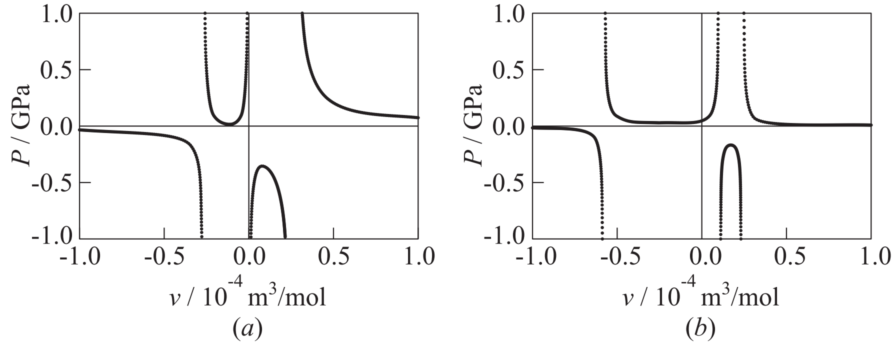

Figure 2 Solution of cubic equations (N_2): (*a*) $T = 600$ K ($T > T_c$), SRK EoS; and (*b*) $T = 77.5$ K ($T < T_c$), PR EoS

Equation (2) is solved using Cardano's method and from a mathematical point of view leads to multiple solutions for density knowing p and T. However, only one mathematical solution actually represents a physical solution. In Fig. 2, pressure is plotted as a function of the molar volume for nitrogen using the SRK or PR EoS. Temperature is fixed at 600 K in Fig. 2*a* and 77.5 K in Fig. 2*b*. From a physical point of view, only positive pressures and molar volume above covolume ($v > b$) should be considered even if the solution is a piecewise function defined on $(-\infty; +\infty)$. With that constraint, in Fig. 2*a*, only one solution is found whereas in Fig. 2*b*, two solutions are still found. To understand the possibility of real solutions all verifying $v > b$, one may compare the shape of experimentally obtained curves for $p = f(v)$ at a fixed temperature to the ones obtained with the cubic approximation (Fig. 3). Equation (2) is found unable to represent the Maxwell's thermodynamic surface encounters when the pressure reaches its saturation value (p_s). Then, two or three values of v are the solutions of Eq. (2). To overcome this limitation of the cubic approximation, the following approach is retained in case of multiple solutions all greater than v:

- if $p < p_s$, the smallest value of v is retained (liquid phase, V_A in Fig. 3);
- if $p > p_s$, the largest value of v is retained (gas phase, V_B in Fig. 3); and
- if $p = p_s$, an arbitrary choice is made as the largest value of v is retained.

This means that the phase transition is not properly accounted for in the present approach of real gases thermodynamics and that the results obtained for values of the pressure close to saturation might be erroneous.

To determine the saturation pressure, two approaches have been tested. In Lee–Kesler method [5], p_s is estimated based on critical temperature and pressure as well as the acentric factor:

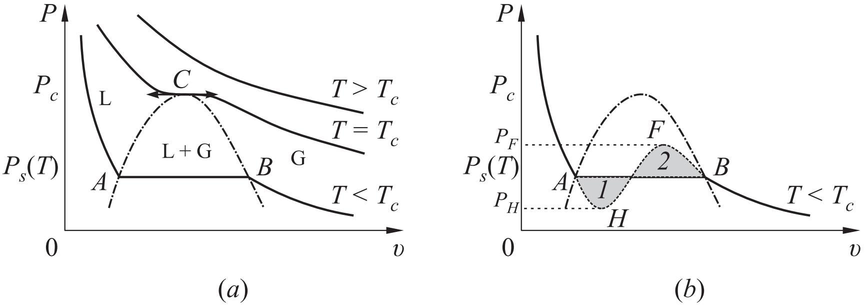

Figure 3 Liquid-gas phase change diagram: (*a*) experimental results (L — liquid; G — gas; and *C* — critical point); and (*b*) cubic approximation: Maxwell's thermodynamic surface

$$\ln(p_{s,r}) = f^{(0)} + \omega f^{(1)}$$

with

$$f^{(0)} = 5.92714 - 6.09648\, T_r^{-1} - 1.28862 \ln(T_r) + 0.169347\, T_r^6\,;$$
$$f^{(1)} = 15.2518 - 15.6875\, T_r^{-1} - 13.4721 \ln(T_r) + 0.43577\, T_r^6\,.$$

The second method uses Maxwell's thermodynamic surface to determine p_s. From thermodynamic considerations, the Gibbs energy, G, is constant along the process of boiling/evaporation: $G(A) = G(B)$ in Fig. 3. Following now the isothermal curve given by the cubic equation (path *AHFB* in Fig. 3*b*), Gibbs energy variation gives:

$$\int\limits_{AB} dG = \int\limits_{AB} V\,dP \iff \Big[VP\Big]_A^B = \int\limits_A^B P\,dV$$
$$\iff P_{\mathrm{sat}}\,(V_A - V_B) = \int\limits_A^B P\,dV\,. \qquad (3)$$

In Fig. 3*b*, Eq. (3) is equivalent to draw a plateau of saturation corresponding to the considered temperature in order to equal the surfaces *1* and *2*. This equation is solved through an iterative Newton procedure.

The comparisons of these two techniques are summarized in Table 3 and compared to experimental data for the saturated vapor pressure of nitrogen. Maxwell's thermodynamic surface provides clearly better results than Lee–Kesler's method. However, in the simulations presented in section 4, the pressure is well above the critical pressure and this situation will not be encountered. Still,

Table 3 Estimation of the saturated vapor pressure of nitrogen

Temperature, K	p_{exp}, kPa	$p_{\mathrm{Lee-Kesler}}$, kPa	ϵ_r, %	p_{Maxwell}, kPa	ϵ_r, %
100	800	940	17.5	790.105	1.2
94	500	644.595	28.9	497.628	0.5
77.5	100	172.47	72.4	89.901	10.1

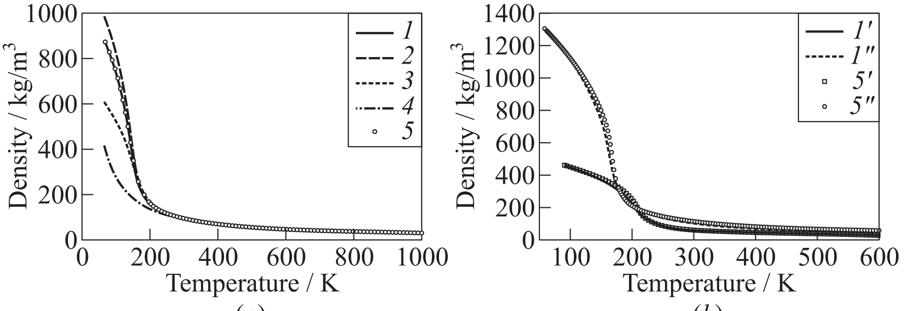

(*a*) (*b*)

Figure 4 Evaluation of cubic EoS (*1* — SRK; *2* — PR; *3* — VDW; and *4* — PG) for density calculation and comparison with NIST data [9] (*5*), $p = 8.0$ MPa: (*a*) N_2 species and (*b*) CH_4 (*1′* — SRK and *5′* — NIST) and O_2 species (*1″* — SRK and *5″* — NIST)

further studies would be required to really quantify the impact of description of flows with transition phase based on cubic EoS.

To analyze the behavior of the cubic EoS in detail, several simulations have been performed for nitrogen, methane, and oxygen. In Fig. 4*a*, density of nitrogen is estimated through the VDW, SRK, PR, and PG EoS and compared with NIST data [9] for a large range of temperature (100 to 2000 K) for a fixed pressure of 8.0 MPa. As expected, VDW and PG EoS are not able to yield a good estimation of density in the low-temperature zone. The SRK EoS follows NIST data over the entire range of temperature. This point is also confirmed in Fig. 4*b* for methane and oxygen density. Similarly, the saturated vapor pressure for nitrogen is computed with VDW, SRK, and PR EoS for temperature ranging from 77.5 to 122.5 K and compared with NIST data (Fig. 5). Once again, SRK EoS gives better results with a relative error lower than 10%. The VDW EoS is clearly not able to recover NIST data. For the species under study, SRK EoS is found superior to PR EoS. However, Kim *et al.* recently showed that a three-parameter EoS coupling SRK and PR leads to better results for kerosene/LOx combustion than the only use of SRK or PR EoS [10].

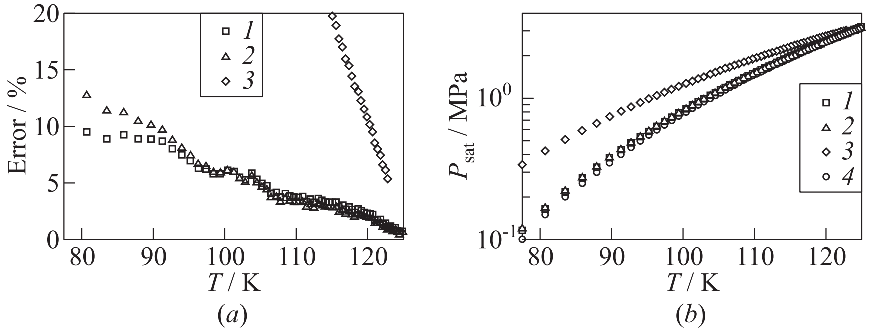

Figure 5 Relative error ϵ_r (*a*) of saturated vapor pressure of nitrogen, $P_s^{\text{N}_2}$ (*b*): *1* — SRK EoS; *2* — PR EoS; *3* — VDW EoS; and *4* — NIST

2.2 Mixing Rules, Thermodynamic and Transport Properties

Dealing with supercritical multispecies fluid flows requires adapted mixing rules. In Eq. (1), the coefficients $a\alpha$ and b are replaced by $(a\alpha)_m$ and b_m following the rules of VDW [5]:

$$(a\alpha)_m = \sum_i \sum_j X_i X_j \sqrt{a_i a_j \alpha_i \alpha_j}(1 - \kappa_{ij}); \qquad b_m = \sum_i X_i b_i \,.$$

Hirschfelder *et al.* [11] proposed slightly different expressions:

$$(a\alpha)_m = \sum_i \sum_j X_i X_j \sqrt{a_i a_j \alpha_i \alpha_j}(1-\kappa_{ij}); \; b_m = \sum_i \sum_j X_i X_j \left[\frac{1}{2}(b_i^{1/3} + b_j^{1/3})\right]^3$$

where X_k is the mole fraction of species k and κ_{ij} are the binary interaction coefficients [12] between species i and j. The constants a_i, b_i, and α_i are determined from the universal relationships given in Table 2 where T_c and p_c are, respectively, replaced by T_{c_i} and p_{c_i}, the critical temperature and pressure of species.

Changing EoS modifies thermodynamic properties of mixture. Indeed, pressure effects have to be taken into account and thermodynamic properties such as enthalpy, h, internal energy, e, entropy, s, or heat capacities, C_p, must be temperature and pressure dependent. One possible implementation is based on departures functions (DEP) that are defined as the difference between the property of interest in its real state and its ideal gas state (0). As a consequence, any property M can be written as:

$$M = M_0 + M^{\text{DEP}} \,.$$

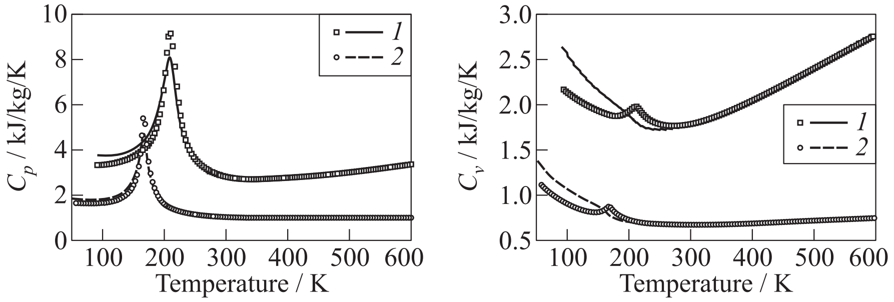

(*a*) (*b*)

Figure 6 Comparison of calculated heat capacities based on SRK EoS (curves) and experimental data from NIST (symbols) for CH_4 (*1*) and O_2 species (*2*) at 8.0 MPa: (*a*) $C_p(T)$; and (*b*) $C_v(T)$

Such properties are expressed as:

$$e(T,\rho) = e_0(T) + \int\limits_{\rho_0}^{\rho} \left[\frac{p}{\rho^2} - \frac{T}{\rho^2} \left(\frac{\partial p}{\partial T} \right)_\rho \right]_T d\rho\,;$$

$$h(T,P) = h_0(T) + \int\limits_{p_0}^{p} \left[\frac{1}{\rho} + \frac{T}{\rho^2} \left(\frac{\partial p}{\partial T} \right)_p \right]_T dp\,;$$

$$s(T,\rho) = s_0(T,\rho_0) - \int\limits_{\rho_0}^{\rho} \left[\frac{1}{\rho^2} \left(\frac{\partial p}{\partial T} \right)_\rho \right]_T d\rho\,;$$

$$C_p(T,\rho) = C_{v_0} - \int\limits_{\rho_0}^{\rho} \left[\frac{T}{\rho^2} \left(\frac{\partial^2 p}{\partial T^2} \right)_\rho \right]_T d\rho + \frac{T}{\rho^2} \frac{(\partial p/\partial T)_\rho^2}{(\partial p/\partial \rho)_T}$$

with C_{v_0} the ideal gas heat capacity at constant volume.

Heat capacities (C_p and C_v) of methane and oxygen evaluated at 8.0 MPa with SRK EoS and compared to experimental data from NIST are plotted in Fig. 6. A fairly good agreement is found. An error around 10% is found when crossing the pseudoboiling line (PBL) (peak in Fig. 6) for C_p and C_v. The PBL represents the prolongation of the gas/liquid phase-change line and corresponds to a maximum of constant-pressure heat capacity for a given pressure. Finally, error in Fig. 6 is found much more pronounced where the fluid is dense, i. e., when the temperature is below the peak of PBL. In addition, the absolute amount of error for C_v is the same that on C_p, but is more apparent since C_v is much smaller.

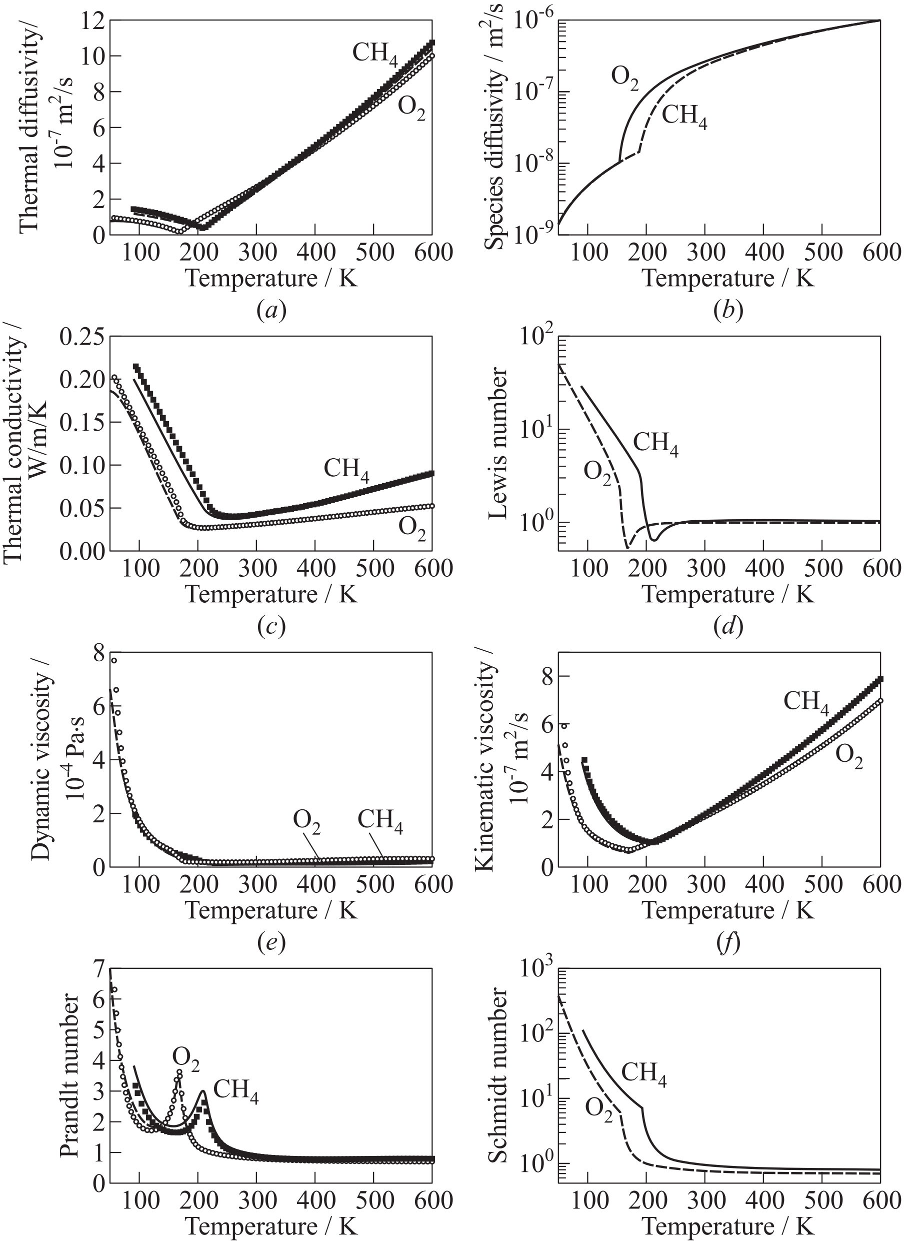

Figure 7 Comparisons between SRK EoS (curves) and NIST data (symbols) for viscosity, conductivity, and diffusivity. Empty signs refer to O_2 and filled signs to CH_4

Classical techniques used to evaluate transport properties (viscosity and thermal conductivity) can be replaced by the accurate high-pressure relations proposed by Chung *et al.* [13], which extends the Chapman–Enskog theory by introducing a dense-fluid correction. The binary mass diffusivity may be predicted by the Takahashi method [14] or follow recommendations given by Bellan [3]. All these models incorporate features that are inherent to molecular level description: electrostatic interactions, asymmetrical distribution of charges (if any), polarizability, dispersion forces or VDW-like attraction, and repulsion. In Fig. 7, the evaluation of thermal (a) and species (D_k) diffusivity, thermal conductivity (λ), and dynamic (μ) and kinematic (ν) viscosities as functions of temperature for a pressure set to 8.0 MPa are given using the SRK EoS and compared to available NIST data [9]. Very good agreements are found. In Figs. 7*d* and 7*h*, Schmidt ($\mathrm{Sc}_k = \nu/D_k$) and Lewis ($\mathrm{Le} = \mu C_p/\lambda$) numbers, respectively, exhibit large variations: for low temperatures, both numbers have liquid-like values whereas they have gas-like values when temperature is above 200 and 250 K for O_2 and CH_4, respectively.

3 TRANSPORT EQUATIONS AND NUMERICAL SOLVERS

In this section, transport equations used to simulate the two issues highlighted in introduction, i. e., a supercritical channel flow and a supercritical flow injection, are first presented. Two numerical solvers have been used and will be briefly detailed hereafter. The first one is called here "Georgia Tech. Solver" and is mainly dedicated to Large Eddy Simulations (LES) whereas the second one is called SiTCom-B and is mainly dedicated to Direct Numerical Simulation (DNS).

3.1 Transport Equations

For nonreacting supercritical multispecies flows, the energy, species, and Navier–Stokes equations must be solved together with an appropriate description of the real-gas thermodynamics (see section 2). For multispecies system, Dufour (energy flux due to a mass concentration gradient) and Soret (mass flux due to a temperature gradient) effects should be considered with attention to get the entire description of the flow [15]. However, in a LES context, these effects are generally neglected. Favre filtering instantaneous conservation equations [16] for Cartesian coordinates are summarized below:

- mass:

$$\frac{\partial \overline{\rho}}{\partial t} + \frac{\partial (\overline{\rho}\tilde{u}_i)}{\partial x_i} = 0\,, \quad i \in [1,3]\,;$$

– momentum:

$$\frac{\partial(\overline{\rho}\tilde{u}_i)}{\partial t} + \frac{\partial(\overline{\rho}\tilde{u}_i\tilde{u}_j)}{\partial x_j} = -\frac{\partial p(\bar{\phi})}{\partial x_i} + \frac{\partial \sigma_{ij}(\bar{\phi})}{\partial x_j} + \frac{\partial \tau_{ij}}{\partial x_j} - \frac{\partial}{\partial x_i}[\overline{p} - p(\bar{\phi})]$$

where

$$\sigma_{ij} = \mu(\tilde{T}) \left[\left(\frac{\partial \tilde{u}_i}{\partial x_j} + \frac{\partial \tilde{u}_j}{\partial x_i} \right) - \frac{2}{3}\frac{\partial \tilde{u}_k}{\partial x_k}\delta_{ij} \right]; \qquad \tau_{ij} = \overline{\rho}(\tilde{u}_i\tilde{u}_j - \widetilde{u_i u_j});$$

– species k:

$$\frac{\partial \overline{\rho}\tilde{Y}_k}{\partial t} + \frac{\partial(\overline{\rho u_i Y_k})}{\partial x_i} = -\frac{\partial \bar{j}_{k,i}}{\partial x_i};$$

– energy:

$$\frac{\partial(\overline{\rho}\tilde{e}_t)}{\partial t} + \frac{\partial(\overline{\rho}\tilde{e}_t\tilde{u}_i)}{\partial x_i} = -\frac{\partial p(\bar{\phi})\tilde{u}_i}{\partial x_i} - \frac{\partial q_i}{\partial x_i} + \frac{\partial \sigma_{ij}\tilde{u}_i}{\partial x_i} + \frac{\partial}{\partial x_i}[\overline{\rho}(\tilde{u}_i\tilde{h} - \widetilde{u_i h})] - \frac{\partial(\overline{\rho}\tau_{ij}\tilde{u}_i)}{\partial x_i}$$

where q_i and $j_{k,i}$ represent the heat flux and species mass flux, respectively, to model; and $\phi = (\rho, \rho u_i, \rho e_t)$ with u_i, e_t, and h being the components of the velocity, total energy, and enthalpy, respectively.

From a numerical point of view, supercritical fluid flows may lead to very steep density gradients that must be well captured as they drive the flow phenomenology. This point is a crucial issue of such flows and two dissipative numerical schemes should be discarded.

3.2 Georgia Tech. Solver

Yang's code [4, 17–20] is a preconditioned parallel multiblock flow solver that uses a fourth central (4C) numerical scheme for spatial discretization on generalized curvilinear coordinates. This one is replaced by the WENO relations given in [21] that are general and valid for any EoS. Comparisons with the original 4C scheme leads to sharper and accurate results [21]. The WENO for real gas keeps a formulation similar to that derived with an ideal gas EoS. The fifth-order WENO formulation of Jiang and Shu [22] or the formulation of Taylor *et al.* [23] and Martin *et al.* [24] are available. This latter improves the resolution of very fine flow structures and exhibits a spectral behavior close to fourth-order Padé schemes [24]. Its implementation has already been successfully validated on the Shu–Osher problem [25], a shock focusing phenomenon [26], a homogeneous isotropic turbulence, a compressible turbulent boundary layer [24], and an isothermal wall-bounded channel flow simulation [27]. A fourth-order Runge–Kutta scheme is used to solve the governing equations. Thermodynamic is based on SRK EoS with Chung *et al.* and Takahashi methods for transport properties (see above).

3.3 CORIA Solver

The CORIA Lab recently developed a new version of SiTCom solver called SiTCom-B (Simulation of Turbulent Combustion with Billions of points) [28–32] which is mainly designed to perform DNS and highly resolved LES on thousands of processors. It is a finite-volume code that solves the unsteady compressible reacting Navier–Stokes equations system on Cartesian meshes. The SiTCom-B solver features the following characteristics: forth-order central difference schemes plus artificial dissipation term of the second and fourth order from Tatsumi *et al.* [33], Runge–Kutta time-discretization (third and forth orders), full multispecies formulation, realistic thermodynamic (CHEMKIN), realistic transport properties [11], complex chemistry, tabulated chemistry, ideal or real gas EoS, NSCBC (Navier–Stokes Characteristic Boundary Conditions) boundary treatment [31] and immersed boundary method. For the simulation, presented herein, thermodynamic is based on SRK EoS with Chung *et al.* and Takahashi methods for transport properties as in the Georgia Tech. solver.

From a numerical point of view, both numerical codes (Georgia Tech. and CORIA) are very close, except that SiTCom-B does not use any preconditioning scheme and WENO method. In the following applications, Smagorinsky model has been used to describe the subgrid scale effect of turbulence, Dufour and Soret effects as well as $\partial[\overline{p} - p(\bar{\phi})]/\partial x_i$ are also neglected.

4 EXAMPLES OF APPLICATIONS

Several theoretical and numerical efforts have already been realized to understand supercritical regime phenomena in the past ten years. These studies are relatively recent and their comparison with experiments is limited because the experimental data available are scarce. For example, there is no detailed experimental data on the development of turbulence for mixing layers in a supercritical regime. Thus, Oefelein and Yang [18] used a classical model of turbulence developed for atmospheric pressure conditions to perform a LES of a reactive two-dimensional (2D) shear layer of oxygen/hydrogen under supercritical conditions. The results obtained show that the density gradient between the flow of oxygen and hydrogen drives the evolution of the mixing layer. The same result was also observed with DNS of Miller *et al.* [34, 35], Okong'o *et al.* [36], and Oefelein [37] where the temporal evolution of non-reactive mixing layers of heptane/oxygen and hydrogen/oxygen under supercritical conditions was studied. Only few LES of supercritical flows have been realized (see, for example, [18, 38] or [39, 40]) for the single round nitrogen jet simulation. The stabilizing effect of the density gradient and its role on turbulent energy redistribution along the mixing layer was identified. Oefelein and Yang [18] performed a shear layer liquid oxygen (LOx) / H_2 jet flame at critical pressure and highlighted that the flame stabilization mechanism near the injector lips observed in experiments (see, for example, [41]) is linked to the presence of a strong recirculation zone of burnt gases. Zong and Yang [42] performed a LES of a shear coaxial LOx/CH_4 jet flame at critical pressure and found the same typical behavior of flame in the case of liquid methane injection that it is described by Singla *et al.* [41].

In LRE, LOx is directly injected into the combustion chamber whereas the combustible (mainly, H_2) is first used in the regenerative cooling system before its injection. Cooling the walls of the combustion chamber is crucial for the LRE integrity and accurate estimation of heat transfer, is then the keystone of thermodynamic cycle [43–48]. Clearly, heat transfer and fluid injection are closely linked as injection defines the flame position, i. e., the amount of heat transferred to the cooling system. These two issues are now studied through the LES tools.

4.1 Supercritical Channel Flow Simulation

The target configuration is a pure oxygen stream at $T = 160$ K flowing between two cooled walls, one facing a hot temperature (top) of 600 K, and the other one being adiabatic (bottom). Slip conditions are prescribed on side walls. The bulk velocity is $U_b = 119$ m/s. The inlet turbulence is given by the Klein algorithm, i. e., inflow data for DNS or LES are generated based on a digital filter as explained in [20, 49]. The channel lengths are $L_x = 20$ mm, $L_y = 5$ mm, and $L_z = 2$ mm. Around 72 millions of cells have been used on 576 processors in order to get a fine mesh resolution. A uniform mesh is used for the x and y directions: $\Delta x = 0.041$ mm and $\Delta y = 0.0194$ mm. In the z direction, $\Delta z \approx 0.00176$ mm with a stretched zone in the channel center. Indeed, increasing the pressure decreases the size of the smallest structures [7]. This academic test case mimics the EH3C (Electrically Heated Curved Cooling Channel) test bench [50–52] that is operated at the DLR. The supercritical fluid flowing inside this straight channel will experience a strong heat transfer coming from only one side of the channel wall. Because of experimental characteristics (inlet diameter different from channel diameter, for example), the DLR configuration is a challenge for CFD and the academic configuration is preferred. Reynolds-Average Navier–Stokes simulations have been already done by Pizzarelli *et al.* [53] but this is the first attempt for LES. Georgia Tech. Solver is used for this study.

In Fig. 8, a snapshot of temperature field, taken in the middle of the channel, is given along with the top and bottom Q-criterion isosurfaces for vortices visualization. The Q-criterion is defined as

$$Q = \frac{1}{2}\left(\Omega_{ij}\Omega_{ij} - S_{ij}S_{ij}\right)$$

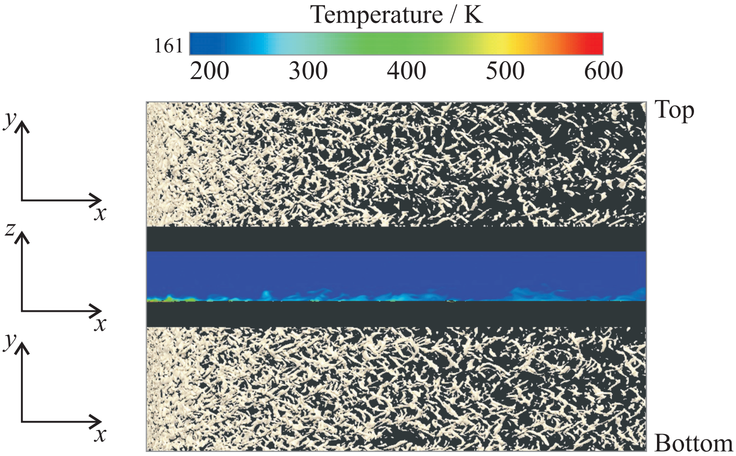

Figure 8 Slice of temperature (middle) and Q-criterion isosurfaces (top and bottom) on the whole domain of calculation ($L_x = 20$ mm, $L_y = 5$ mm, and $L_z = 2$ mm).

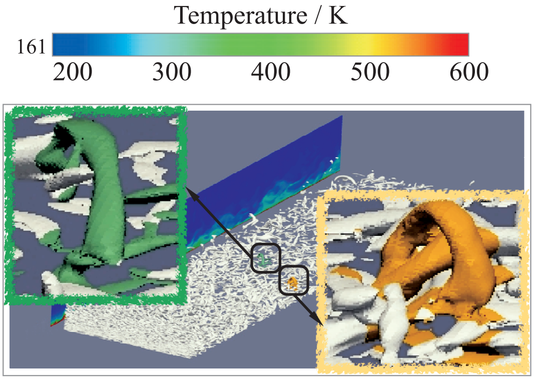

Figure 9 Horseshoe-like structures.

where Ω_{ij} and S_{ij} are the antisymmetric and symmetric parts of the velocity gradient, respectively [54]. In Figs. 8 and 9, Q-criterion isosurfaces are given for $Q = (U_b/L_z)^2$. The cold stream is very dense compared to the fluid coming up to the hot wall. The hot fluid is restrained to a very small portion of the flow very close to the wall. Impact of Klein's method is visible on the first part on the channel where very small structures are synthetically created. Then, mass, momentum, and heat transfers reorganize and lead to classical horseshoe-like structures [55] that are identified in Fig. 9 close to the walls. These structures are

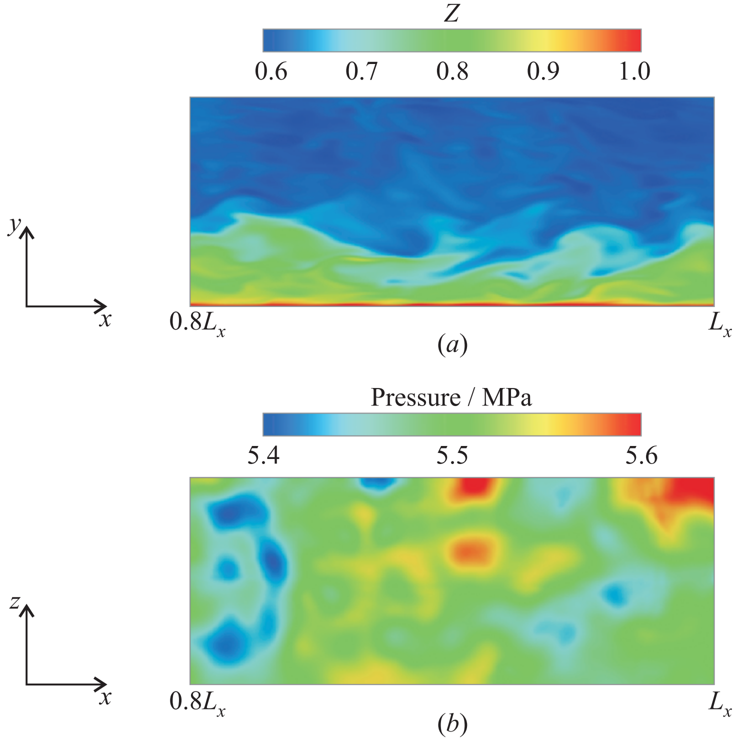

Figure 10 Compressibility (*a*) and pressure fields (*b*) taken at the end of the channel.

responsible of the heat transfer from/to walls. However, their appearance seems to be less frequent compared to what was observed in ideal fluids because of the very thin thickness of the hot fluid. In Fig. 10, compressibility, Z, and pressure fields are shown for the last part of the channel configuration, where Klein's inlet technique has no influence anymore. In Fig. 10*b* (x–z plane), pressure jump does not exceed the mean pressure and then does not get under the critical point of oxygen, thus avoiding to consider multiphase flow modeling. In Fig. 10*a* (x–y plane), impact of real gas effect is visible on compressibility field as a very thin layer of ideal gas-like fluid is located near walls, but quickly interacts with the dense flow above it.

4.2 Supercritical Flow Injection Simulation

The topic addressed in this study focuses on a 2D mixing layer with conditions similar to the one in Mayer's experiment [1, 56] except for the velocity (50 m/s)

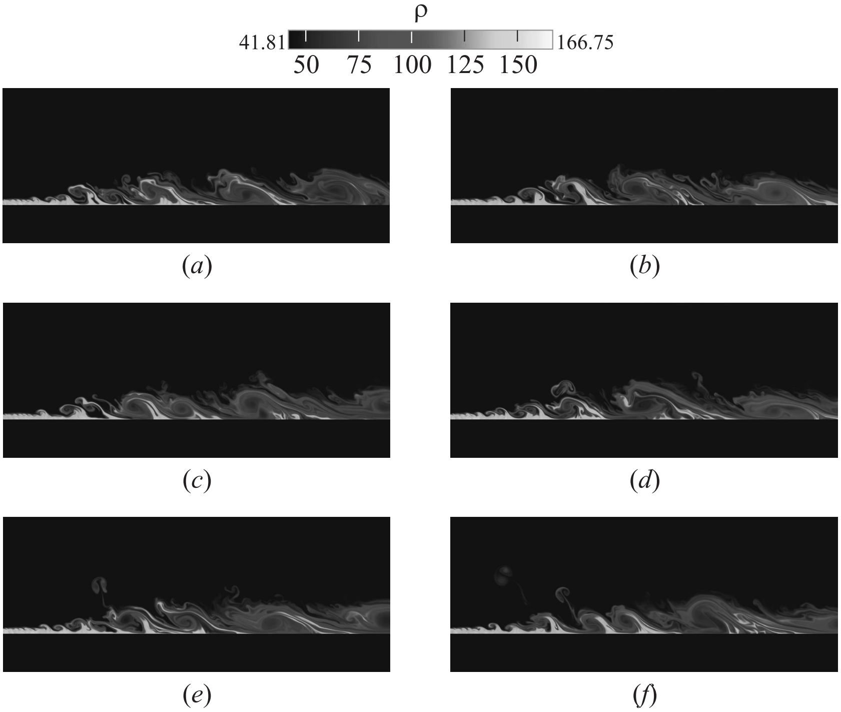

Figure 11 Temporal evolution of density for dense nitrogen jet into warm nitrogen at high-pressure conditions: (*a*) $t = 5.4$ ms; (*b*) 6.08; (*c*) 6.75; (*d*) 7.43; (*e*) 8.1; and (*f*) $t = 9.45$ ms

that is chosen to mimic more realistic injection conditions. Cold nitrogen (137 K) is injected into a warm nitrogen (300 K) environment with a pressure of 4.0 MPa in the chamber. The diameter of the injector is 2.2 mm. The results are displayed in Fig. 11 for different times of calculation. Turbulence injection is clearly visible on figures and allows the flow to destabilize. The mesh discretization is $\Delta x \approx 0.05$ mm (the mesh is stretched at the end of the simulated domain) and $\Delta y = 0.05$ mm; the corresponding domain dimensions are $L_x = 381.23$ mm and $L_y = 30$ mm. SiTCom-B is used for this study.

The density gradient seems well-captured as attested by the presence of very distinct small-scale structures (see Fig. 11). Indeed, the present authors recently simulated the exact Mayer's configuration with three-dimensional (3D) simulations and comparison with mean axial density measurements exhibited a fairly good agreement [40].

The flow field displays very interesting flow structures such as dense vortex detaching from the main jet (Fig. 11*e*) and persisting in the low-speed and light region (Fig. 11*f*). Fluid is denser in the jet core and vortices develop by capturing a pocket of light fluid from the surrounding warm nitrogen before convecting it into the main flow. Then, these vortices with a light core persist on the whole simulated chamber length. Vortex pairing is also observed in Figs. 11*c* and 11*d* where vortices detached themselves from the main jet and create finger-like structures. Size of vortices does not exceed six times the injector radius. When a vortex pairing appears in the inner part of jet, the new vortex is automatically stretched before combining with another vortex. This type of structures has not been retrieved on the round jet at 5 m/s [40] but might be present for the 3D jet at higher velocity.

5 CONCLUDING REMARKS

Dealing with supercritical flows requires a special treatment of thermodynamics and numerics. Thermodynamic has to be based on general relations and appropriated EoS. The SRK and PR cubic EoS may be used with a good level of confidence. However, close to the critical point, further investigations are required as cubic EoS might not be sufficiently accurate around this point. Similarly, if a phase transition occurs, cubic EoS validity has still to be assessed for this new physics. Transport properties are modeled with dense fluid corrections, theories available in literature appear to satisfactorily reproduce data from NIST. Turbulence modeling approaches will have to take into account steep density gradients that naturally occur in LRE cooling channels or injection systems. Thus, the balance between turbulence subgrid modeling and numerical viscosity imposed by the steep gradients will be a keystone of such fluid flows description. Going further with supercritical flows will then require to consider massively parallel simulations allowing for fine grid resolution, in order to really capture the physics [57] without relying too heavily on numerical dissipation [16].

ACKNOWLEDGMENTS

The computations were performed using HPC resources from GENCI [CCRT/CINES/IDRIS] and CRIHAN.

REFERENCES

1. Mayer, W., J. Telaar, R. Branam, G. Schneider, and J. Hussong. 2003. Raman measurements of cryogenic injection at supercritical pressure. *Heat Mass Transfer* 39:709–19.

2. Candel, S., M. Juniper, G. Singla, P. Scouflaire, and C. Rolon. 2006. Structure and dynamics of cryogenic flames at supercritical pressure. *Combust. Sci. Technol.* 178:161–92.
3. Bellan, J. 2000. Supercritical (and subcritical) fluid behavior and modeling: Drops, streams, shear and mixing layers, jets and sprays. *Prog. Energy Combust. Sci.* 26:329–66.
4. Meng, H., and V. Yang. 2003. A unified treatment of general fluid thermodynamics and its application to a preconditioning scheme. *J. Comput. Phys.* 189:277–304.
5. Poling, B. E., J. M. Prausnitz, and J. P. O'Connell. 2001. The properties of gases and liquids. McGraw Hill. 5th ed.
6. Clifford, T. 1999. *Fundamentals of supercritical fluids*. Oxford Science Publication.
7. Yang, V. 2000. Modeling of supercritical vaporization, mixing, and combustion processes in liquid-fueled propulsion systems. *Proc. Combust. Inst.* 28:925–42.
8. Oefelein, J. C. 2005. Thermophysical characteristics of shear-coaxial LOx–H_2 flames at supercritical pressure. *Proc. Combust. Inst.* 30:2929–37.
9. http://webbook.nist.gov.
10. Kim, S.-K., H.-S. Choi, and Y. Kim. 2012. Thermodynamic modeling based on a generalized cubic equation of state for kerosene/LOx rocket combustion. *Combust. Flame* 159:1351–65.
11. Hirschfelder, J., C. Curtiss, and R. Byron Bird. 1964. *Molecular theory of gases and liquids*. New York: Wiley Ed.
12. Graboski, M., and T. Daubert. 1978. A modified Soave equation of state for phase equilibrium calculation. *Ind. Eng. Chem. Proc. Design Development* 17:443–50.
13. Chung, T. H., M. Ajlan, L. L. Lee, and K. E. Starling. 1988. Generalized multiparameter corresponding state correlation for polyatomic, polar fluid transport properties. *Ind. Chem. Eng. Res.* 27:671–79.
14. Takahashi, S. 1974. Preparation of a generalized chart for the diffusion coefficient of gases at high pressures. *J. Chem. Eng. (Japan)* 7:417.
15. Harstad, K., and J. Bellan. 2000. An all-pressure fluid drop model applied to a binary mixture: Heptane in nitrogen. *Int. J. Multiphase Flow* 26:1675–706.
16. Taskinoglu, E., and J. Bellan. 2010. A posteriori study using a DNS database describing fluid disintegration and binary-species mixing under supercritical pressure: Heptane and nitrogen. *J. Fluid Mech.* 645:211–54.
17. Hsieh, S. Y., and V. Yang. 1997. A preconditioned flux-differencing scheme for chemically reacting flows at all Mach numbers. *Int. J. Comput. Fluid Dyn.* 8:31–49.
18. Oefelein, J. C., and V. Yang. 1998. Modeling high-pressure mixing and combustion processes in liquid rocket engines. *J. Propul. Power* 14:843–57.
19. Zong, N., and V. Yang. 2005. An efficient preconditioning scheme for general fluid mixture using primitive variables. *Int. J. Comput. Fluid Dyn.* 21:217–30.

20. Zong, N., H. Meng, S.-Y. Hsieh, and V. Yang. 2006. A numerical study of cryogenic fluid injection and mixing under supercritical conditions. *Combust. Sci. Technol.* 178:193–227.
21. Taieb, D., G. Ribert, and V. Yang. 2011. Supercritical fluid behavior in a cooling channel. AIAA Paper No. 2011-392.
22. Jiang, G. S., and C. W. Shu. 1996. Efficient implementation of weighted ENO schemes. *J. Comput. Phys.* 126:202–28.
23. Taylor, E. M., M. Wu, and M. P. Martin. 2007. Optimization of nonlinear error for weighted essentially non-oscillatory methods in direct numerical simulations of compressible turbulence. *J. Comput. Phys.* 223:384–97.
24. Martin, M. P., E. M. Taylor, M. Wu, and V. G. Weirs. 2006. A bandwidth-optimized WENO scheme for effective direct numerical simulation of compressible turbulence. *J. Comput. Phys.* 220:270–89.
25. Shu, C. W., and S. Osher. 1989. Efficient implementation of essentially non-oscillatory shock-capturing schemes II. *J. Comput. Phys.* 83:32–78.
26. Taieb, D., G. Ribert, and A. Hadjadj. 2010. Numerical simulations of shock focusing over concave surfaces. *AIAA J.* 48:1739–47.
27. Taieb, D., G. Ribert, and A. Hadjadj. 2010. DNS and LES of wall-bounded compressible turbulent flows in narrow cooling channel. AIAA Paper No. 2010-638.
28. Domingo, P., L. Vervisch, and K. Bray. 2002. Partially premixed flamelets in LES of nonpremixed turbulent combustion. *Combust. Theory Model.* 6(4):529–51.
29. Domingo, P., L. Vervisch, S. Payet, and R. Hauguel. 2005. DNS of a premixed turbulent V flame and LES of a ducted flame using a FSD-PDF subgrid scale closure with FPI-tabulated chemistry. *Combust. Flame* 143:566–86.
30. Domingo, P., L. Vervisch, and D. Veynante. 2008. Large-eddy simulation of a lifted methane jet flame in a vitiated coflow. *Combust. Flame* 152:415–32.
31. Lodato, G., L. Vervisch, and P. Domingo. 2008. Three-dimensional boundary conditions for direct and large-eddy simulation of compressible viscous flows. *J. Comput. Phys.* 227:5105–43.
32. http://www.coria-cfd.fr/index.php/SiTCom-B.
33. Tatsumi, S., L. Martinelli, and A. Jameson. 1995. Flux-limited schemes for the compressible Navier–Stokes equations. *AIAA J.* 33(2):252–61.
34. Miller, R., and J. Bellan. 1998. Direct numerical simulation of a confined three-dimensional gas mixing layer with one evaporating hydrocarbon-droplet laden stream. *J. Fluid Mech.* 384:293–338.
35. Miller, R., and J. Bellan. 2001. Direct numerical simulations of supercritical fluid mixing layers applied to heptane-nitrogen. *J. Fluid Mech.* 436:1–39.
36. Okong'o, N., K. Harstad, and J. Bellan. 2002. Direct numerical simulations of O_2/H_2 temporal mixing layers under supercritical conditions. *AIAA J.* 40:914–26.
37. Oefelein, J. C. 2006. Mixing and combustion of cryogenic oxygen–hydrogen shear-coaxial jet flames at supercritical pressure. *Combust. Sci. Tech.* 178:229–52.

38. Zong, N., and V. Yang. 2004. Cryogenic fluid jets and mixing layers in transcritical and supercritical environments. *Phys. Fluids* 16(12):4248–61.
39. Schmitt, T., L. Selle, A. Ruiz, and B. Cuenot. 2010. Large-eddy simulation of supercritical-pressure round jets. *AIAA J.* 48(9):2133–44.
40. Petit, X., G. Ribert, and P. Domingo. 2012. Large eddy simulation of supercritical fluid injection. AIAA Paper No. 2012-1268.
41. Singla, G., P. Scouflaire, C. Rolon, and S. Candel. 2005. Transcritical oxygen/transcritical or supercritical methane combustion. *Proc. Combust. Inst.* 30:2921–28.
42. Zong, N., and V. Yang. 2007. Near-field flow and flame dynamics of LOx/methane shear-coaxial injector under supercritical conditions. *Proc. Combust. Inst.* 3:2309–17.
43. Woschnak, A., and M. Oschwald. 2001. Thermo- and fluidmechanical analysis of high aspect ratio cooling channels. AIAA Paper No. 2001-3404.
44. Suslov, D., A. Woschnak, J. Sender, and M. Oschwald. 2003. Test specimen design and measurement technique for investigation of heat transfer processes in cooling channels of rocket engines under real thermal conditions. AIAA Paper No. 2003-4613.
45. Woschnak, A., M. Suslov, and M. Oschwald. 2003. Experimental and numerical investigations of thermal stratification effects. AIAA Paper No. 2003-4615.
46. Pioro, I., H. Khartabil, and R. Duffey. 2004. Heat transfer to supercritical fluids flowing in channels — empirical correlations (survey). *Nuclear Eng. Design* 230:69–91.
47. Parris, D., and D. Landrum. 2005. Effect of tube geometry on regenerative cooling performance. AIAA Paper No. 2005-4301.
48. Locke, J. M., and D. B. Landrum. 2008. Study of heat transfer correlations for supercritical hydrogen in regenerative cooling channels. *J. Propul. Power* 24:94–103.
49. Klein, M., A. Sadiki, and J. Janicka. 2003. A digital filter based generation of inflow data for spatially developing direct numerical or large eddy simulations. *J. Comput. Phys.* 186:652–65.
50. Torres, Y. 2008. Heat and mass transfer in curvatures of cooling channels of rocket engine. Ph.D. University of Valenciennes.
51. Quering, K., W. Zeiss, D. Wiedmann, O. Knab, Y. Torres, and D. Suslov. 2009. Numerical and experimental studies of heat transfer in asymmetrically heated cooling channels. *3rd European Conference for Aerospace Science (EUCASS).*
52. Torres Y., D. Suslov, and O. Haidn. 2009. Nitrogen two-phases in regenerative cooling channels of rocket engine. *3rd European Conference for Aerospace Science (EUCASS).*

53. Pizzarelli, X., N. Francesco, R. Paciorri, and M. Onofri. 2009. Numerical analysis of three-dimensional flow of supercritical fluid in asymmetrically heated channels. *AIAA J.* 47(11):2534–43.
54. Dubief, Y., and F. Delcayre. 2000. On coherent-vortex identification in turbulence. *J. Turbulence* 1:1–22.
55. Coleman, G., J. Kim, and R. Moser. 1995. A numerical study of turbulent supersonic isothermal-wall channel flow. *J. Fluid Mech.* 305:159–83.
56. Oschwald, M., and A. Schik. 1999. Supercritical nitrogen free jet investigated by spontaneous Raman scattering. *Exp. Fluids* 27:497–506.
57. Ribert, G., N. Zong, V. Yang, L. Pons, N. Darabiha, and S. Candel. 2008. Counterflow diffusion flames of general fluids: Oxygen/hydrogen mixtures. *Combust. Flame* 154:319–30.